Available online at www.sciencedirect.com
ScienceDirect
Trans. Nonferrous Met. Soc. China 35(2025) 1787−1802
Transactions of Nonferrous Metals Society of China
www.tnmsc.cn

Dynamic recrystallization behavior and spinning texture formation mechanism of magnesium alloy wheel hub

Bing-chun JIANG[1,2*], Hao-wei ZHAI[3*], Qing-hang WANG[3,4], Meng LI[4], Tong ZHANG[1,2], Bin JIANG[5]

1. School of Mechanical and Electrical Engineering, Guangdong University of Science and Technology, Dongguan 523083, China;
2. Faculty of Digital of Science and Technology, Macau Millennium College, Macau 999078, China;
3. School of Mechanical Engineering, Yangzhou University, Yangzhou 225127, China;
4. CITIC Dicastal Co., Ltd., Qinhuangdao 066000, China;
5. National Engineering Research Center for Magnesium Alloys, College of Materials Science and Engineering, Chongqing University, Chongqing 400044, China

Received 27 June 2024; accepted 26 December 2024

Abstract: The dynamic recrystallization (DRX) behavior and texture formation mechanism in an AZ31 magnesium alloy wheel hub during the spinning process were investigated. Analysis using optical microscopy, electron backscatter diffraction, transmission electron microscopy, and finite element simulation revealed that continuous dynamic recrystallization (CDRX) and grain boundary bulging occurred simultaneously throughout the spinning process, leading to an increased proportion of DRXed grain areas. The newly formed DRXed grains largely retained the orientations of their deformed parent grains. The spinning process had two stages: initially, deformation was driven by basal $\langle a \rangle$ slip as the roller contacted the alloy and descended to its lowest point. In the later stage, pyramidal $\langle c+a \rangle$ slips became predominant as additional force was applied along the spinning direction (SD), forming a final texture with the *c*-axis tilting ±15° towards the SD. This texture development led to discernible anisotropy in tensile properties along the SD and the tangential direction (TD).

Key words: magnesium alloy wheel hub; dynamic recrystallization; spinning texture; dislocation slip; mechanical anisotropy

1 Introduction

In response to global energy challenges, the demand for innovative lightweight materials has steadily increased. Magnesium (Mg) alloys have emerged as a promising area of research due to their low density, exceptional noise reduction, and superior damping properties [1,2]. These advantages position Mg alloys as leading contenders in the next generation of lightweight materials, offering substantial potential in both transportation and aerospace sectors. Notably, in the automotive industry, replacing traditional materials with Mg alloys can lead to a significant 70% reduction in vehicle weight, thus contributing to more sustainable and eco-friendly solutions [3].

Currently, commercial Mg alloys like AZ31, AZ80, and AZ91 are favorable for their affordability and adequate mechanical characteristics, and they are commonly employed in automotive instrument panels and steering wheels [4,5]. Some researchers

* Bing-chun JIANG and Hao-wei ZHAI contributed equally to this work
Corresponding author: Qing-hang WANG, Tel: +86-18883725047, E-mail: wangqinghang@yzu.edu.cn
https://doi.org/10.1016/S1003-6326(25)66783-5

have fabricated Mg wheels through backward extrusion, and further investigated their microstructures and mechanical properties [6−8]. For example, JIANG et al [8] analyzed the revolution of physical field of AZ80 Mg wheel during the backward extrusion, and the analysis result revealed that the rim of the wheel sustained bidirectional compressive stress and unidirectional tensile stress, while its bottom was subjected to the state of three-directional compressive stress. However, the backward extrusion approach exhibited notable manufacturing flaws and low production efficiency. The spinning process, noted for its short production cycle, high precision, and cost-efficiency, has attracted significant interest. This technique is particularly advantageous for manufacturing axisymmetric parts, such as Mg alloy wheel hubs, thereby improving material properties and lowering costs [9].

Recent studies have explored various aspects of the spinning process. BI et al [10] investigated the spinning forming process for automotive rims, optimizing parameters with DEFEROM-3D software. LIANG et al [11] examined the stress−strain distribution during the hot spinning of AZ80 alloy, noting the effects of temperature and thinning rate on material hardness and deformation capacity. XU et al [12] developed a novel ring roll spinning technique to optimize force dynamics, thereby enhancing both the production efficiency and mechanical properties. MURATA et al [13] found that spinning at temperatures above the recrystallization threshold improved material formability and tensile strength due to work hardening. While existing studies have focused on the impact of spinning parameters (e.g., temperature, thinning rate and feed rate [10−13]) on the macroscopic mechanical properties of Mg alloy wheel hubs, microstructural evolution and underlying formation mechanisms during spinning remain largely unexplored.

This work aims to investigate the microstructure evolution of an AZ31 Mg alloy wheel hub throughout the spinning process, with a focus on understanding the mechanisms of dynamic recrystallization (DRX) and the formation of spinning texture, as well as revealing the impact of spinning texture on mechanical anisotropy. This work offers valuable theoretical guidance for the engineering applications of Mg alloy wheel hubs.

2 Experimental

2.1 Material preparation

A commercial AZ31 alloy was used in this study. The as-cast AZ31 bar was forged into the wheel hub through two passes at 400 °C, resulting in a wall thickness of 10 mm, an inner diameter of 400 mm, and a height of 150 mm. Figure 1(a) shows the spinning process of the as-forged wheel hub, and the longitudinal image of the corresponding as-spun sample is exhibited in Fig. 1(b). The spinning deformation was conducted using a spinning machine. The spinning temperature was maintained at 400 °C, and the mold was heated to the same temperature. In order to ensure the temperature stability during the spinning process, a flamethrower was used for temperature compensation. The rotational speed of the mandrel, the feed rate and the thinning rate were 400 r/min, 2 mm/s and 70% (total reduction in 7 mm), respectively. Figure 1(c) shows the schematic diagram of the spinning process. The regions of microstructural observation located at the longitudinal section of the as-spun sample, which were marked by red boxes 1−4 along the spinning direction (SD).

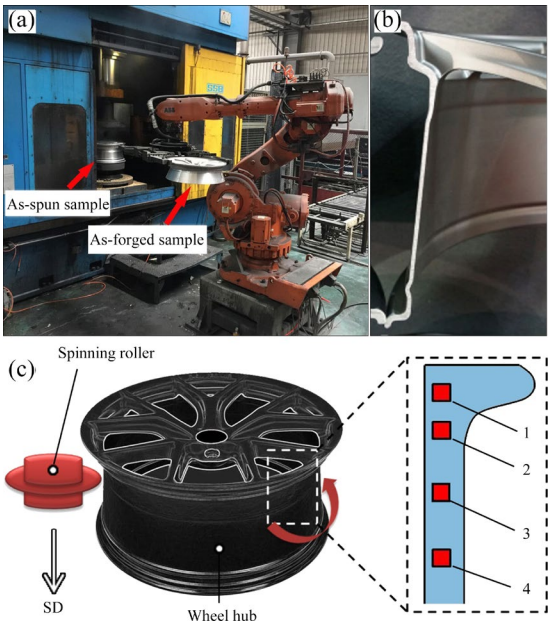

Fig. 1 Spinning process illustrating transition from as-forged sample to as-spun sample (a), longitudinal view of corresponding as-spun sample (b), and schematic diagram during spinning process, including regions of microstructural observation marked by red boxes 1−4 along SD (c)

2.2 Microstructural measurements and tensile tests

The microstructures of all samples were analyzed by optical microscopy (OM, ZEISS Axiovert 40 MAT), electron backscatter diffraction (EBSD, JEOL JSM−7800F) technique and transmission electron microscopy (TEM, FEI TECNAI G2 F20). The EBSD samples were electro-polished with AC2 at 20 V, 0.03 A and −30 °C for 75 s. The scanning step was set to be 0.5 μm. All EBSD data were analyzed using Channel 5 software. The foils for TEM observations were prepared by mechanical polishing them to 50 μm and then punched into disks (3 mm in diameter). Subsequently, the treated foils were further thinned to 30 nm by ion beam using GATAN-PIPS 691 device. The SD- and tangential direction (TD)-tensioned samples (10 mm × 5 mm × 3 mm in gauge length, width and thickness, respectively) were machined from the AZ31 wheel hub and measured using a CMT6305-300 kN universal testing machine at room temperature and strain rate of 1×10^{-3} s^{-1}. Three tensile samples were tested under each condition to guarantee the reproducibility of experiments.

2.3 Finite element simulation

In order to study the force states of wheel hub during the spinning process, the commercial Abaqus/Explicit software was used to establish a single-pass spinning model. During the finite element simulation (FEM), the following assumptions were made for the model to improve the computational efficiency and accuracy [11]: (1) the billet was simplified as tubing without a bottom. This simplification reduced the complexity of the model while maintaining the essential characteristics needed to study the spinning process; (2) the billet was set as an isotropic elastic-plastic material, i.e., it had identical mechanical properties in all directions and could undergo both elastic and plastic deformation. The spinning roller and the mandrel were modeled as rigid bodies to reduce computational effort since their changes were negligible compared to the billet; (3) the inner and outer surfaces of the billet were lubricated with graphite to simulate the actual lubrication conditions during spinning. The friction law applied to the surface contact between the spinning roller and the mandrel was penalty friction, with a friction coefficient of 0.3. The AZ31 material was characterized by specifying the fundamental material properties and applying an Arrhenius constitutive model incorporated via a user-defined material subroutine.

Figure 2 shows the FEM model of spinning. In order to improve the prediction accuracy, the workpiece dimensions and spinning parameters in the FEM were aligned with those used in the actual experiment. The FE cylinder model was meshed by linear reduced-integral cells (C3D8R), comprising three layers of meshes along the normal direction (ND), 40 meshes along the SD, and 168 meshes along the TD, for a total of 20160 meshes. C3D8R cells are commonly used for sever plastic deformation simulations because they are well-suited to nonlinear problems, offer high computational efficiency, and prevent locking phenomena. Here, the mandrel was fixed so that the spinning roller rotated along the mandrel to achieve the spinning process in the FEM. During the deformation, the mesh was prone to aberration, so it was necessary to turn on the mesh adaptive technology so that the mesh was automatically adjusted to divide the mesh when the workpiece and the spinning roller were in contact. The starting point of the spinning roller was set below the bottom surface of the workpiece. The spinning roller was then fed axially by a single-segment motion, while the thinning rate was controlled by adjusting the distance between the spinning roller and the workpiece's outer surface.

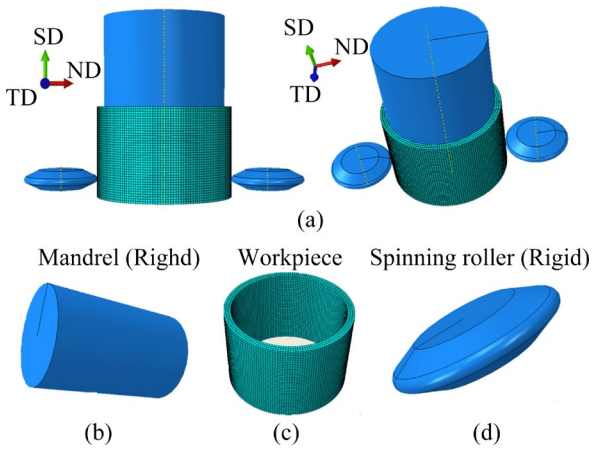

Fig. 2 FEM model of spinning process including three parts (a), mandrel (b), workpiece (c) and spinning roller (d)

3 Results and discussion

3.1 Microstructure

Figure 3 presents the OM images of an AZ31 wheel hub at various positions (Positions 1−4) in Fig. 1(c) throughout the spinning process. Initially, at Position 1 (Fig. 3(a)), the sample, akin to its as-forged state, consists of a mixture of fine and coarse grains, with their area fractions at approximately 26.2% and 73.8%, respectively. As the spinning process advances, there is a gradual increase in the area fraction of fine grains due to the DRX behavior, whereas coarse grains stretch along the SD, resulting in a decreased area fraction (Figs. 3(b−d)). At Position 4, the area fractions of fine and coarse grains stabilize at about 40.3% and 59.7%, respectively (Fig. 3(d)).

Figure 4 illustrates the EBSD analysis results of the AZ31 wheel hub at Positions 1, 2 and 4 in Fig. 1(c). This analysis confirms the mixed grain structure observed in OM images, which remains consistent across all samples. With the progression of the spinning process, there is a noticeable reduction in the average grain size from 17.6 μm at Position 1 to 5.8 μm at Position 4 (Figs. 4(a−c)). These findings further confirm that DRX occurs during the spinning process. To distinguish the DRXed grains from unDRXed regions, grains with a grain orientation spread (GOS) below 2° are considered DRXed ones [14]. Figures 4(d−f) depict the DRXed grains at Positions 1, 2, and 4, respectively, revealing a continuous increase in the DRXed grain area fraction from about 24.7% at Position 1 to approximately 35.4% at Position 4, accompanied by a corresponding decrease in unDRXed regions. Notably, some fine grains are classified as unDRXed regions because they continue to undergo deformation during the spinning process [15,16].

The (0001) pole figures at Positions 1, 2, and 4 are displayed in Figs. 4(j−l), respectively. Initially, the as-forged sample at Position 1 exhibits a texture with most grain *c*-axes inclined at ±33° and ±7° to the SD and the TD, respectively. This texture type resembles that of the unDRXed regions, even though the DRXed grains exhibit a more dispersed and weaker texture (Fig. 4(j)). Previous studies [17−19] highlighted the significant impact of DRX on texture weakening. As the process moves to Position 2, the inclination angle between the *c*-axis and TD narrows to approximately 0° from ±7°, introducing a new texture component with the *c*-axis inclined at ±27° to the SD and a slight drop in texture intensity from 13.8 to 11.9 (Fig. 4(k)).

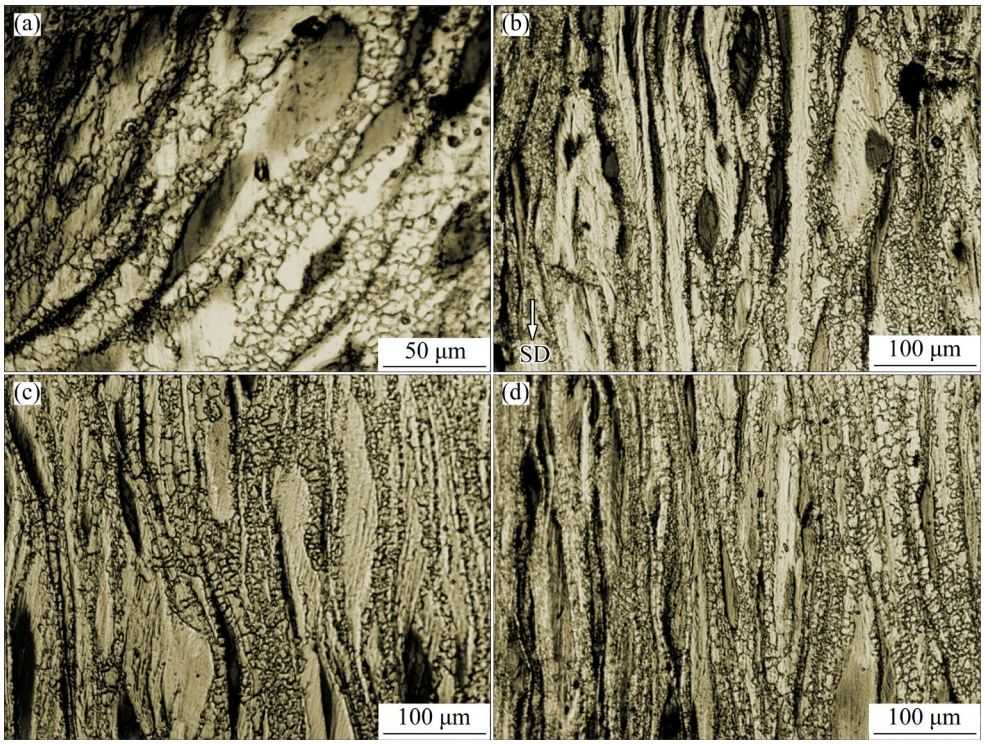

Fig. 3 OM images of AZ31 wheel hub at different positions in Fig. 1(c) during spinning process: (a) Position 1 (Position 1 represents forged state); (b) Position 2; (c) Position 3; (d) Position 4

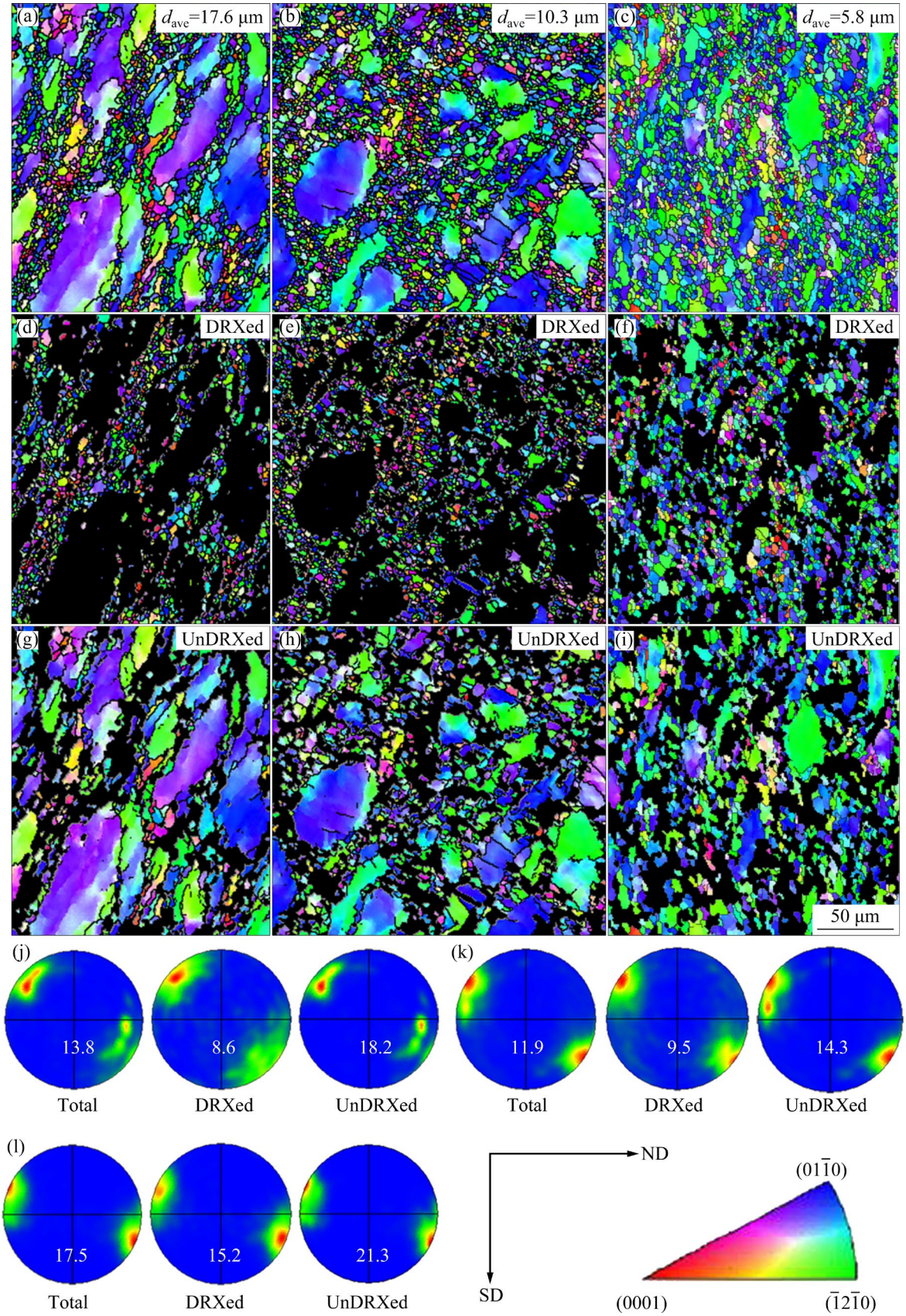

Fig. 4 EBSD analysis results of AZ31 wheel hub at different positions in Fig. 1(c) during spinning process: (a−c) Inverse pole figures (IPFs) at Positions 1, 2 and 4, respectively; (d−f) Extracted DRXed grains from (a−c), respectively; (g−i) Remained unDRXed regions from (a−c), respectively; (j−l) (0001) pole figures at Positions 1, 2 and 4, respectively

At Position 4, the SD-inclined angle further reduces to ±15° (Fig. 4(l)), which was also reported in a ZK60 alloy after the spinning process [20]. Contrary to expectations, DRX does not continue to diminish texture intensity at this stage; instead, it rises to 17.5. Moreover, at Positions 2 and 4, the texture features of the DRXed grains and unDRXed regions are similar, suggesting that the crystal orientations of newly formed grains inherit those of the parent grains, closely associated with the DRX behavior during the spinning process.

3.2 DRX mechanism

It is well known that DRX mechanisms can be divided into the continuous dynamic recrystallization (CDRX) and discontinuous dynamic recrystallization (DDRX) [15−20]. CDRX involves the rearrangement of dislocations during the deformation to form low-angle grain boundaries (LAGBs), which then absorb more dislocations, evolving into high-angle grain boundaries (HAGBs) [21]. DDRX, on the other hand, typically nucleates at the locations like grain boundaries, secondary phases, twins, and shear bands [18,22−24].

To gain deeper insight into the DRX mechanisms occurring in the AZ31 wheel hub during the spinning process, a specific area from Position 2, as shown in Figs. 1(c) and 4(b), is examined, with the area of interest being highlighted in Fig. 5. In Fig. 5(a), a distinct colorful gradient within a deformed parent grain (marked as P) is visible, surrounded by 21 newly-formed small grains (labeled G1−G21). The kernel average misorientation (KAM) map in Fig. 5(b) shows that these G1−G21 grains have extremely low average KAM values (below 0.05°), identifying them as new DRXed grains [18]. In contrast, the P grain, with a significantly higher average KAM value (over 1.5°), is considered as an unDRXed grain. Analyzing the cumulative misorientation angle along arrow A→B within the P grain reveals a transition exceeding 10° (Figs. 5(c) and (d)), indicating that LAGBs have converted into HAGBs, a hallmark of the CDRX process. Misorientation angle distribution maps at Positions 1 and 2 (Fig. S1 in Supplementary Materials) show a decrease in LAGB proportion ($2°<\theta<10°$) from ~33.2% to ~30.7%, and an increase in HAGB proportion ($\theta\geq10°$) from ~66.8% to ~69.3%, further confirming CDRX via LAGB consumption. Additionally, Figs. 5(a−c) illustrate some DRXed grains (G1−G21) nucleating at the boundary of P

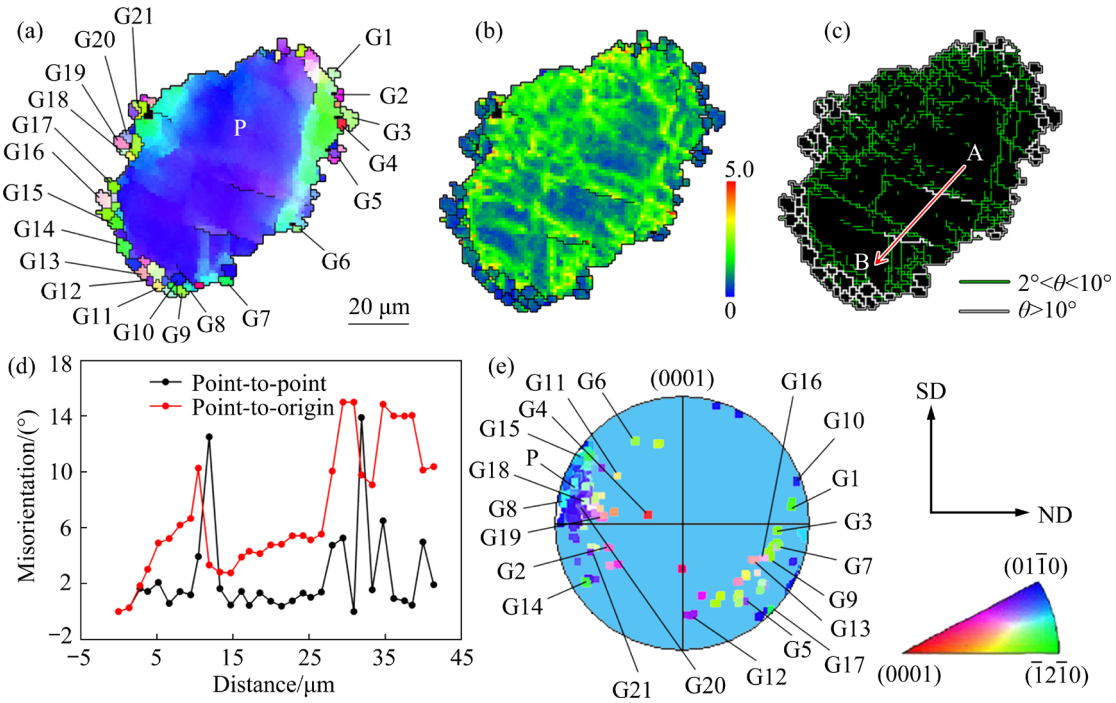

Fig. 5 DRX mechanism analysis results at Position 2 in Fig. 1(c): (a) IPF map including parent grain (P) and 21 grains (G1−G21); (b) Corresponding KAM map; (c) Boundary map; (d) Line profiles of point-to-point and point-to-origin along red arrow A→B; (e) (0001) pole figure from (a)

grain through original flat boundary migration to regions of high dislocation density, thereby forming a crystalline core. This process, known as grain boundary bulging nucleation due to the strain-induced boundary migration (SIBM) [18,25−27], is a characteristic DDRX mechanism. LUO et al [28] also observed a similar phenomenon where dislocations accumulated near the unDRXed region boundaries, creating a local strain gradient that drove the nucleation of DDRX during the extrusion of a dilute Mg−0.5Bi−0.5Sn (wt.%) alloy.

Figure 5(e) reveals the crystal orientations of the parent grain (P) and the newly developed DRXed grains (G1−G21) on the (0001) pole figure. Most of G1−G21 grains exhibit crystal orientations similar to that of the P grain, suggesting the inheritance of crystal orientations from the unDRXed parent grain to the new DRXed grains. Our previous researches [21,29] and other studies [30−32] indicated that the slip-induced strain gradient within the unDRXed regions tends to promote the formation of new grains with orientations similar to that of the parent grain via CDRX. However, the impact of DDRX on texture development remains unclear. For instance, generally, the particle-stimulated nucleation (PSN) mechanism is known to facilitate the nucleation of grains with random orientations [22]. Twin-induced DDRX mechanism plays a vital role in forming rare-earth (RE) textures in wrought RE/Ca-containing alloys [23,33]. SANJARI et al [34] observed the SIBM mechanism in an annealed Mg−4Zn−1Ce (wt.%) alloy, where grain boundary bulging from neighboring deformed grains towards high-energy regions led to the nucleation of new grains with orientations similar to their parent grains [30,34,35]. At Position 2, the combined effect of CDRX and DDRX via grain boundary bulging results in a texture similarity between the DRXed grains (G1−G21) and the deformed parent grain (P).

As the spinning process advances to Position 4, the area fraction of DRXed grains increases (Fig. 4(c)). The DRX behavior at this stage, depicted in Fig. 6, involves 17 fine DRXed grains (labeled by G1−G17) surrounding a deformed

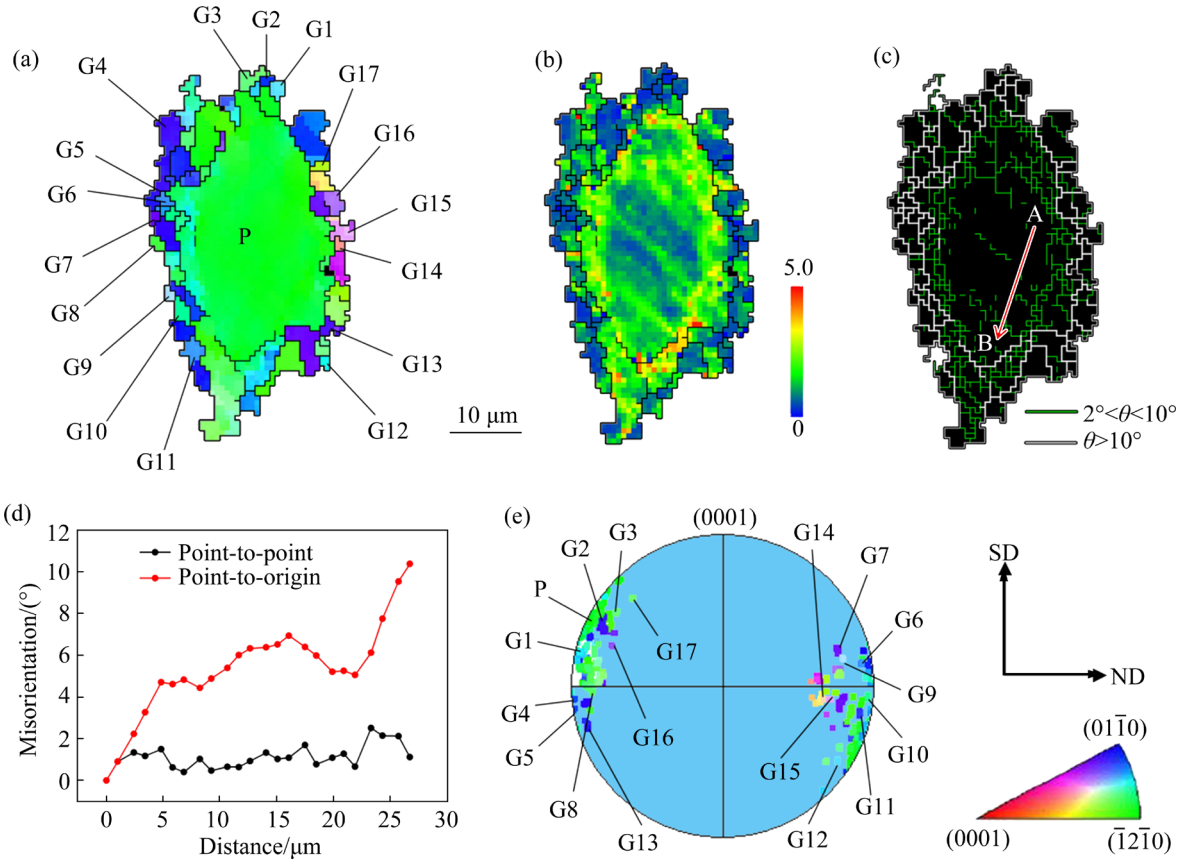

Fig. 6 DRX mechanism analysis results at Position 4 in Fig. 1(c): (a) IPF map including parent grain (P) and 17 grains (G1−G17); (b) Corresponding KAM map; (c) Boundary map; (d) Line profiles of point-to-point and point-to-origin along red arrow A→B; (e) (0001) pole figure from (a)

parent grain (P). The cumulative misorientation angle along arrow A→B exceeds 10° (Figs. 6(c) and (d)), indicating the presence of the CDRX mechanism via an orientation gradient. The occurrence of the DDRX mechanism is also suggested by the grain boundary bulging nucleation of G1−G17 grains around the P grain (Fig. 6(a)), similar to earlier observations. From Positions 2 to 4, the CDRX and DDRX mechanisms via grain boundary bulging dominate the DRX behavior. The (0001) pole figure in Fig. 6(e) shows a similar crystal orientation between the P grain and most DRXed grains (G1−G17), aligning with findings from Fig. 5(e), primarily due to the combined effect of both DRX mechanisms. This orientation inheritance contributes to the strengthening of the overall texture intensity.

Figure 7 presents a schematic diagram of the DRX behavior of the AZ31 wheel hub during the spinning process to clarify the microstructure evolution. Initially, the as-forged sample contains a certain amount of fine DRXed and coarse unDRXed grains. Throughout the spinning process, both CDRX and DDRX mechanisms are activated at high temperatures. Dislocations rearrange into LAGBs, absorb more dislocations into sub-grain boundaries, and eventually transform into HAGBs. Concurrently, grain boundaries from neighboring deformed grains bulge towards high-energy regions under the SIBM mechanism, forming a crystalline core. This process leads to a gradual increase in the area fraction of DRXed grains and a decrease in the unDRXed regions in the as-spun sample.

3.3 Formation of spinning texture

In Section 3.2, the microstructure evolution and the DRX behavior of the AZ31 wheel hub during the spinning process were systematically explored. In this section, the origin of the spinning texture is further unveiled. Figure 8(a) illustrates the equivalent strain distribution of the AZ31 wheel hub during the spinning process, as determined by FEM. The process is categorized into two stages: The first step (0−5 s) begins when the spinning roller contacts the workpiece and ends at the thinnest point along the ND. The second step (5−26 s) involves applying additional force along the SD. At the 5 and 26 s marks, corresponding to Positions 2 and 4, respectively, Grids 1 and 2 (highlighted with red boxes) are analyzed. These grids experience three normal strains (ε_{TD-TD}, ε_{ND-ND}, and ε_{SD-SD}) and three shear strains (γ_{ND-SD}, γ_{SD-TD}, and γ_{ND-TD}), with their values presented in Figs. 8(b) and (c). For Grid 1, ε_{ND-ND} (−0.369, indicating compressive strain) is the most significant, surpassing ε_{TD-TD} (0.158) and ε_{SD-SD} (0.179), and γ_{ND-TD} (−0.246, indicating clockwise shear strain) exceeds γ_{ND-SD} (0.039) and γ_{SD-TD} (0.068). These results show that the principal strains at Position 2 (illustrated in Fig. 8(d)) are ε_{ND-ND} and γ_{ND-TD}. For Grid 2, ε_{ND-ND} (−0.353) remains predominant over ε_{TD-TD} (0.117) and ε_{SD-SD} (0.134), but γ_{ND-SD} (−0.468) is the most significant, outdoing γ_{SD-TD} (0.041) and γ_{ND-TD} (−0.136). This indicates that at Position 4 (depicted in Fig. 8(e)), the principal strains are ε_{ND-ND} and γ_{ND-SD}.

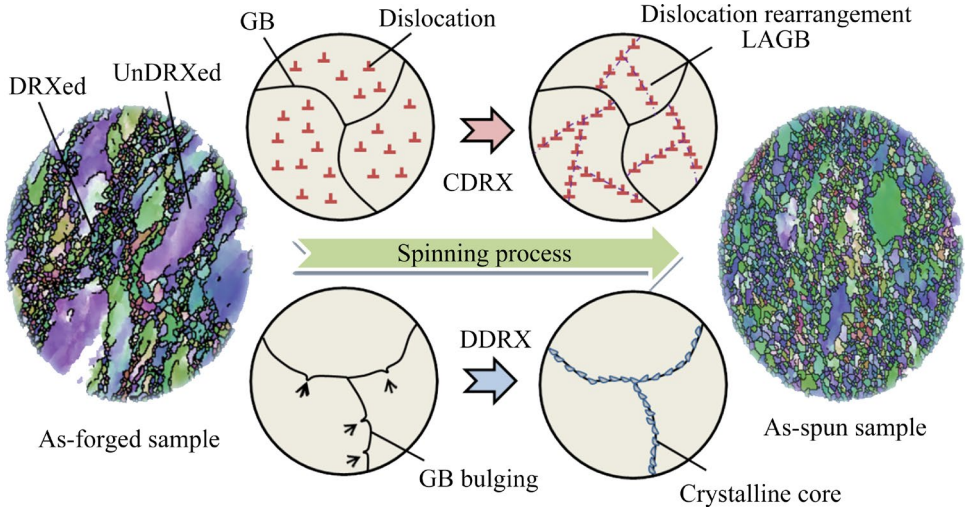

Fig. 7 Schematic diagram of DRX behavior of AZ31 wheel hub during spinning process

When grains in Mg and its alloys are subjected to external forces, slip and/or twinning deformation mechanisms are activated to accommodate the strains. Basal ⟨*a*⟩ slip, due to its relatively low critical resolved shear stress (CRSS), is the most readily activated slip system in these materials [36], as depicted in Fig. 9(a). The activation of this slip system results in the rotation of the *c*-axis of grain parallel to the direction of the applied force, contributing to the formation of basal texture during

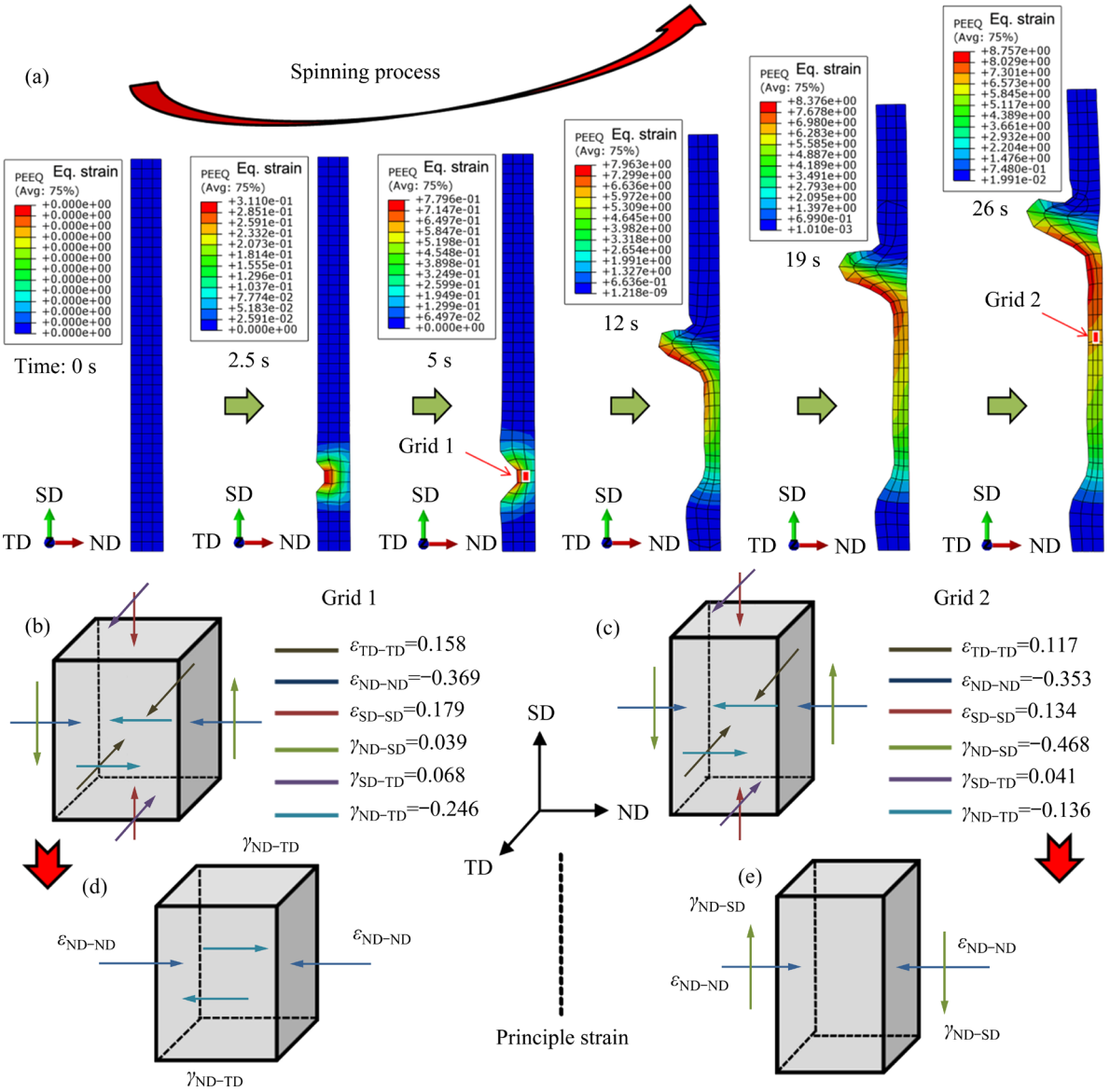

Fig. 8 Equivalent strain distribution of AZ31 wheel hub during spinning process through FEM (a), equivalent strain (b, c) and principle strains (d, e) analysis results in Grids 1 and 2, respectively

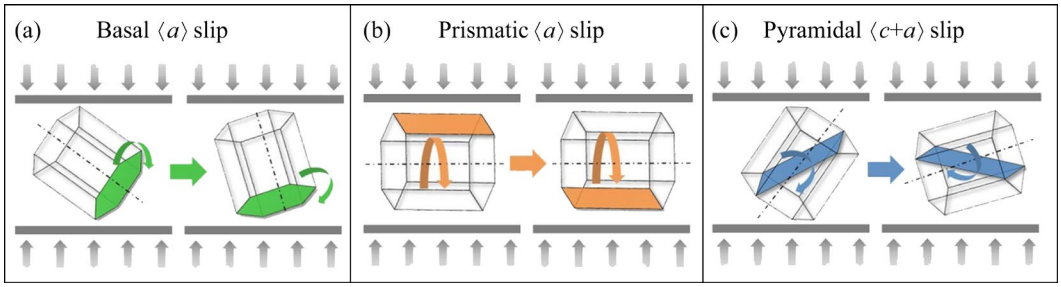

Fig. 9 Schematic diagrams of activated slip modes when grain is applied external forces: (a) Basal ⟨*a*⟩ slip; (b) Prismatic ⟨*a*⟩ slip; (c) Pyramidal ⟨*c*+*a*⟩ slip

the extrusion and/or rolling processes [37,38]. Figure 9(b) shows prismatic ⟨*a*⟩ slip, which involves the rotation of the *a*-axis of grain around its *c*-axis, leaving the texture component on the (0001) pole figure unchanged. The addition of Li decreases the *c*/*a* ratio, enhancing prismatic ⟨*a*⟩ slip activity in Mg−Li alloys [39,40]. In contrast, pyramidal ⟨*c*+*a*⟩ slip demands higher temperatures because its CRSS is roughly 100 times greater than that of basal ⟨*a*⟩ slip in pure Mg [36]. As a result, it drives the *c*-axis of the grain to incline perpendicularly to the applied force direction, as shown in Fig. 9(c). In this study, the contribution of twinning to texture formation is considered negligible, particularly at high temperatures [41], as little to no evidence of twinning was observed during the spinning process (Figs. 3 and 4).

To establish the relationship between texture and slip modes under external forces, Fig. 10 demonstrates grain rotation across different slip modes during the spinning process, simplified into two stages (from Position 1 to Position 2 (Fig. 10(a)) and from Position 2 to Position 4 (Fig. 10(b)). Texture is defined as the orientation of a grain in the

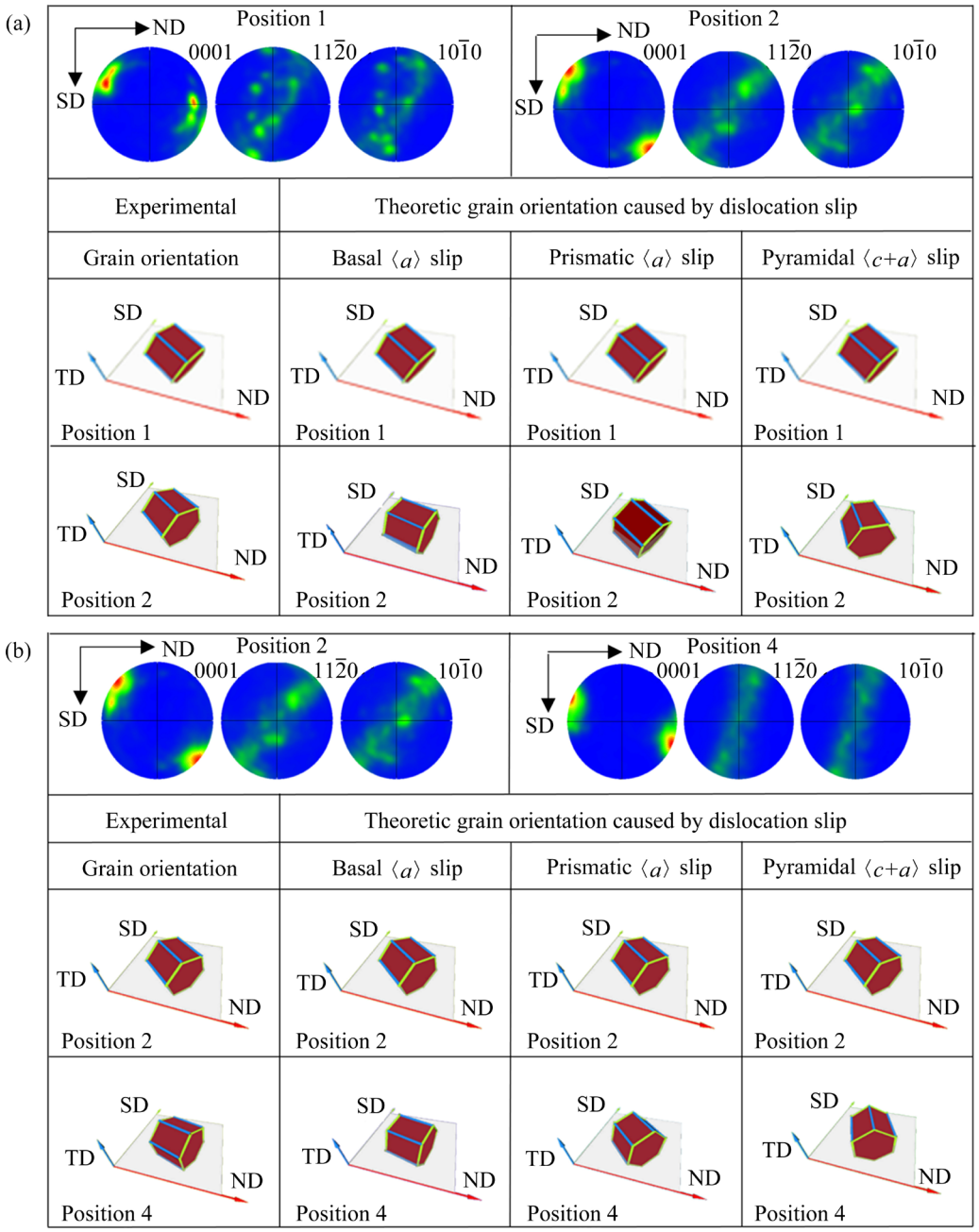

Fig. 10 Grain rotation at different slip modes during spinning process: (a) From Position 1 to Position 2; (b) From Position 2 to Position 4

area of maximum pole intensity. In this study, actual changes in grain orientation were observed experimentally. The theoretical grain orientations, resulting from different dislocation slip modes (basal $\langle a\rangle$, prismatic $\langle a\rangle$ and pyramidal $\langle c+a\rangle$ slips), are compared with the experimental results. If the experimental grain orientations align closely with the theoretical ones, the slip system will be the dominant factor in the spinning process. At Position 2, where the workpiece mainly experiences ε_{ND-ND} and γ_{ND-TD} strains, basal $\langle a\rangle$ slip activity inclines the c-axis of the grain towards the ND as the process moves from Position 1 to Position 2. Meanwhile, prismatic $\langle a\rangle$ slip results in the a-axis rotating around its c-axis. If pyramidal $\langle c+a\rangle$ slip occurs, the c-axis of grain will move away from the ND toward the SD. Based on the texture at Position 2, basal $\langle a\rangle$ slip is predicted to dominate from Position 1 to Position 2, with prismatic $\langle a\rangle$ slip also activated, as evidenced by increased pole intensity on the $(10\bar{1}0)$ pole figure [42,43]. Due to challenging to confirm, the activation of pyramidal $\langle c+a\rangle$ slip, less favorable for texture formation at Position 2, needs further examination via TEM (see Fig. 11).

As the spinning process transitions from Position 2 to Position 4, the workpiece primarily undergoes ε_{ND-ND} and γ_{ND-SD} strains at Position 4, as depicted in Fig. 8(e). According to the grain rotation criteria illustrated in Fig. 9, the c-axis of grain should continue to incline towards the ND due to the activity of basal $\langle a\rangle$ slip. However, this inclination is not pronounced, suggesting that significant non-basal slip activities are involved. The lack of noticeable intensification in pole intensity on the $(11\bar{2}0)$ and/or $(10\bar{1}0)$ pole figures indicates that prismatic $\langle a\rangle$ slip activity is relatively weak. Consequently, the activation of pyramidal $\langle c+a\rangle$ slip becomes essential to cause the c-axis of grain to diverge from the ND.

In order to further verify the results of the applied force analysis, Fig. 11 shows the TEM dark-field images of the sample at Positions 2 and 4 using two-beam diffractions including g=0001 and $g=10\bar{1}0$. All images are associated with the $[2\bar{1}\bar{1}0]$ zone axis. The $g\cdot b$ (g and b represent reciprocal and magnitude of Burgers vectors, respectively) rule is usually used to judge the types of slip systems [44]. When the value of $g\cdot b$ is not equal to 0, dislocations are visible. In contrast, as

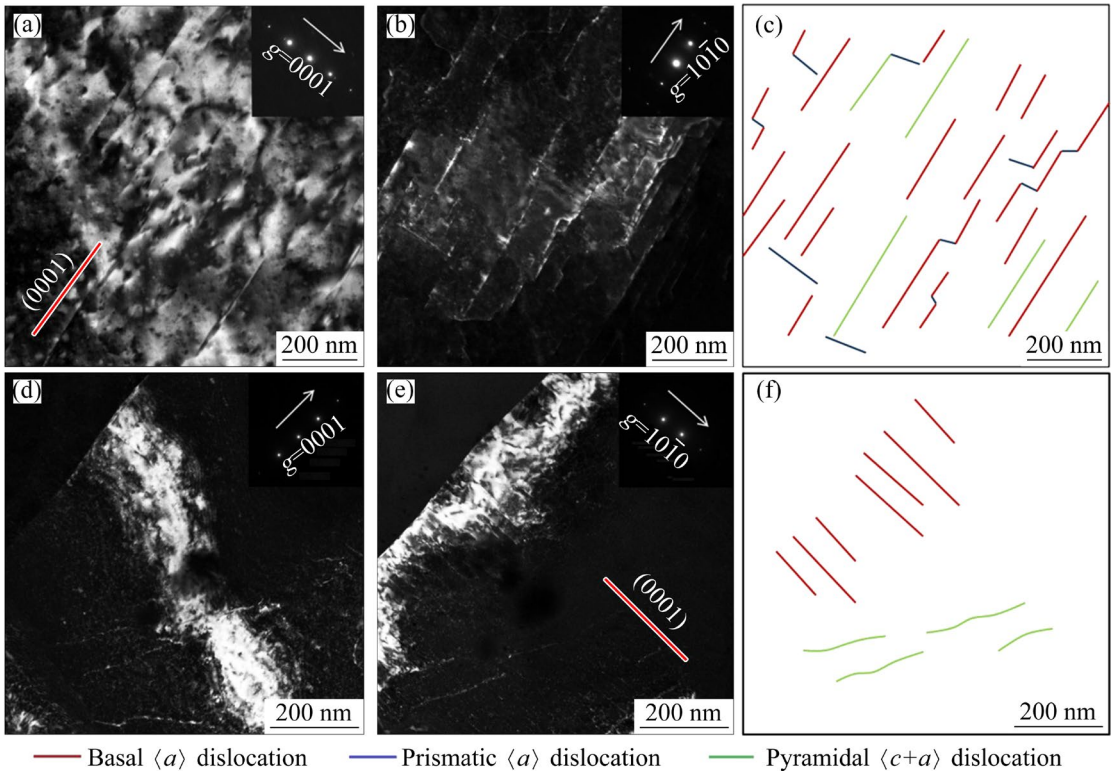

Fig. 11 TEM dark-field images of sample at Position 2 (a−c) and Position 4 (d−f) using two-beam diffractions including g=0001 and $g=10\bar{1}0$

the value of $g \cdot b$ is equal to 0, the dislocation is invisible. Under g=0001 the ⟨a⟩ dislocations are invisible due to $g \cdot b$=0, while the ⟨c+a⟩ and ⟨a⟩ dislocations can be found ($g \cdot b \neq 0$). Under $g=10\bar{1}0$ the ⟨a⟩ dislocations disappear via $g \cdot b$=0, but the partial ⟨a⟩ and ⟨c+a⟩ dislocations are visible ($g \cdot b \neq 0$).

At Position 2, long-straight dislocation lines parallel to the (0001) plane, observable under g=0001 (Fig. 11(a)), are also visible under $g=10\bar{1}0$ (Fig. 11(b)). These dislocations are identified as pyramidal ⟨c+a⟩ screw dislocations, indicated by green lines in the schematic diagram of Fig. 11(c). Additionally, numerous long-straight dislocation lines parallel to the (0001) plane and a few short cross-slip dislocation lines perpendicular to the (0001) plane are observed under $g=10\bar{1}0$ (Fig. 11(b)). Based on the $g \cdot b \neq 0$ criterion, these are identified as basal ⟨a⟩ dislocations (marked in red in Fig. 11(c)) and prismatic ⟨a⟩ dislocations (marked in blue), respectively. Statistical analysis reveals the line densities of basal ⟨a⟩, prismatic ⟨a⟩, and pyramidal ⟨c+a⟩ dislocations to be approximately 68.8%, 8.9%, and 22.3%, respectively. This confirms that basal ⟨a⟩ slip is the predominant deformation mode from Position 1 to Position 2, with only minor contributions from prismatic ⟨a⟩ and pyramidal ⟨c+a⟩ slips.

At Position 4, there is an increase in long, straight dislocation lines aligned parallel to the (0001) plane, visible under g=0001 (Fig. 11(d)) and $g=10\bar{1}0$ (Fig. 11(e)), indicating the presence of pyramidal ⟨c+a⟩ dislocations (highlighted by green lines in Fig. 11(f)). However, in contrast to the observations at Position 2 (Fig. 11(b)), no cross-slip dislocation lines are detected under $g=10\bar{1}0$ at Position 4. Except for pyramidal ⟨c+a⟩ dislocations, numerous basal ⟨a⟩ dislocations are noted, identifiable as the long-straight lines parallel to the (0001) plane under $g=10\bar{1}0$. Statistical analysis shows line densities of basal ⟨a⟩ and pyramidal ⟨c+a⟩ dislocations at about 58.7% and 41.3%, respectively. Thus, in addition to basal ⟨a⟩ slip, a significant increase in pyramidal ⟨c+a⟩ slip activity contributes to the final spinning texture formation, resulting in the c-axis inclining ±15° towards the SD.

3.4 Mechanical anisotropy

In Sections 3.2 and 3.3, the microstructure evolution of AZ31 wheel hub during the spinning process and the formation mechanism of spinning texture have been analyzed. In this section, the tensile properties of AZ31 wheel hub were tested along the SD and TD, and the effect of microstructure on the tensile properties was further discussed.

Figure 12(a) shows the schematic diagram of SD- and TD-tensioned samples from the AZ31 wheel hub, and Fig. 12(b) displays their engineering tensile stress−strain curves along with the corresponding tensile properties. Both the samples display a typical slip-dominated convex curve. The SD-tensioned sample has a lower yield tensile strength (YTS, about 186.3 MPa), but higher ultimate tensile strength (UTS, about 296.5 MPa) and elongation-to-failure (EL, about 20.1%) compared to the TD-tensioned sample, which shows values of approximately 209.1 MPa, 289.4 MPa, and 14.7%, respectively. Obviously, the AZ31 wheel hub shows the planner anisotropy of tensile properties along the SD and TD.

In general, alloying concentration, grain structure, grain size, texture, and the presence of secondary phases are pivotal in influencing the mechanical properties of Mg alloys [45,46]. In this study, texture stands out as the primary factor causing planar anisotropy in tensile properties. Basal slip, which is more readily activated during room-temperature deformation than other slip modes in Mg alloys [36], plays a significant role. Figures 12(c) and (d) present the Schmid factor (SF) maps for basal slip in the samples subjected to tension along the SD and TD, respectively, with average SF values calculated and shown in Figs. 12(e) and (f). The SD-oriented spinning texture results in a higher SF for basal slip (0.26) in the SD-tensioned sample compared to that of the TD-tensioned sample (0.18). High SF values for basal slip are widely recognized as indicators of low yield strength, enhanced ductility, and increased work-hardening capacity in Mg alloys [45]. The mechanical responses of both the SD- and TD-tensioned samples align well with the SF criterion. As a result, the difference of SF for basal slip directly leads to the occurrence of the planner anisotropy of tensile properties along the SD and TD.

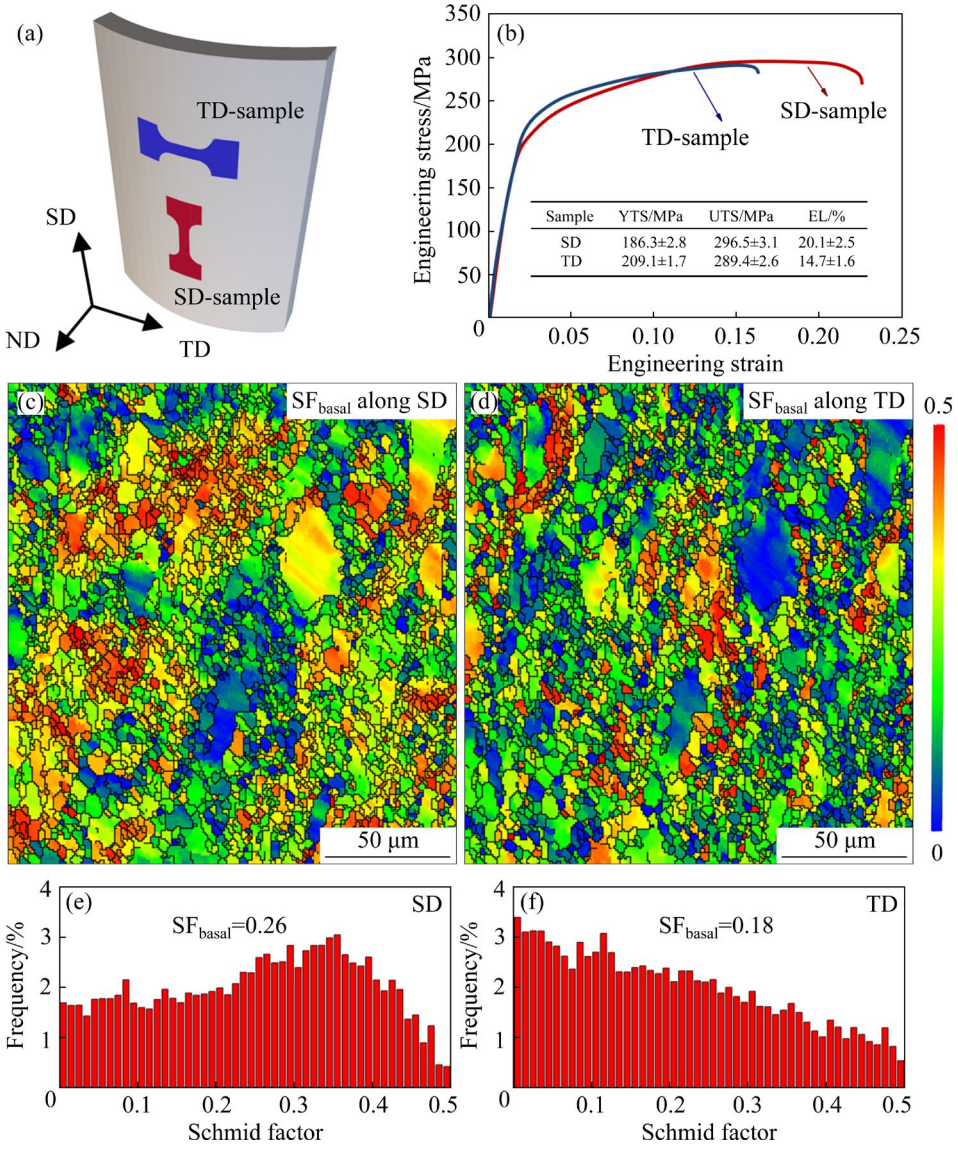

Fig. 12 (a) Schematic diagram of SD- and TD-tensioned samples at Position 4 from AZ31 wheel hub; (b) Corresponding engineering tensile stress−strain curves; (c−f) SF maps for basal slip (c, d) and corresponding average SF values (e, f) of samples tensioned along SD and TD, respectively

4 Conclusions

(1) With the advancement of the spinning process, both CDRX and grain boundary bulging mechanisms occur simultaneously, thus increasing the area fraction of DRXed grains. Moreover, the orientations of the DRXed grains largely inherit those of the deformed parent grains.

(2) The spinning process can be divided into two distinct deformation stages: the workpiece predominantly experiences ε_{ND-ND} and γ_{ND-TD} strains, with basal $\langle a \rangle$ slip serving as the primary deformation mechanism, accompanied by minor non-basal slip activities; the principal strains are ε_{ND-ND} and γ_{ND-SD}. Under these conditions, in addition to basal $\langle a \rangle$ slip, there is significant activation of pyramidal $\langle c+a \rangle$ slips, ultimately forming the final spinning texture in which the c-axis of most grains inclines by ±15° toward the SD .

(3) The formation of spinning texture results in planar anisotropy of tensile properties along the SD and TD in the AZ31 wheel hub. The sample tensioned in the SD direction exhibits a lower YTS (~186.3 MPa) but a higher UTS (~296.5 MPa) and EL (~20.1%), compared to the TD-tensioned sample, which achieves approximately 209.1 MPa, 289.4 MPa, and 14.7%, respectively.

CRediT authorship contribution statement

Bing-chun JIANG and **Hao-wei ZHAI:** Preparation, Experiment, Data analysis, Writing − Original draft; **Qing-hang WANG:** Data analysis, Funding acquisition, Writing − Review & editing; **Meng LI:** Preparation, Experiment; **Tong ZHANG:** Preparation, Experiment, Writing − Review & editing; **Bin JIANG:** Writing − Review & editing.

Declaration of competing interest

The authors declare that they have no known competing financial interests or personal relationships that could have appeared to influence the work reported in this paper.

Acknowledgments

This research was funded by the National Natural Science Foundation of China (No. 52204407), the Natural Science Foundation of Jiangsu Province, China (No. BK20220595), and the China Postdoctoral Science Foundation (No. 2022M723689).

Supplementary Materials

Supplementary Materials in this paper can be found at: http://tnmsc.csu.edu.cn/download/05-p1787-2024-0902-Supplementary_Materials.pdf.

References

[1] WANG Qing-hang, JIANG Bin, CHEN Dao-lun, JIN Zhao-yang, ZHAO Ling-yu, YANG Qing-shan, HUANG Guang-sheng, PAN Fu-sheng. Strategies for enhancing the room-temperature stretch formability of magnesium alloy sheets: A review [J]. Journal of Materials Science, 2021, 56: 12965−12998.

[2] JIANG Bin, DONG Zhi-hua, ZHANG Ang, SONG Jiang-feng, PAN Fu-sheng. Recent advances in micro-alloyed wrought magnesium alloys: Theory and design [J]. Transactions of Nonferrous Metals Society of China, 2022, 32: 1741−1780.

[3] MASOOD CHAUDRY U, TEKUMALLA S, GUPTA M, JUN T S, HAMAD K. Designing highly ductile magnesium alloys: Current status and future challenges [J]. Critical Reviews in Solid State and Materials Sciences, 2022, 47: 194−281.

[4] EDOZIUNO F O, ADEDIRAN A A, EMEREJE P O, AKALUZIA R O, JEN T C. Development of lightweight, creep resistant Mg−Zn−Al alloys for automotive applications: Influence of micro-additions of quaternary elements [J]. Results in Engineering, 2024, 21: 101632.

[5] POWELL B R, KRAJEWSKI P E, LUO A A. Materials, design and manufacturing for lightweight vehicles [M]. 2nd ed. New York: Woodhead Publishing, 2021.

[6] JIANG Yan-chao, LIAO Qi-yu, LE Qi-chi, ZHU Ya-tong, YIN Zhao-yang, HU Cheng-lu, LIU Li-chen. Die structure optimization study for magnesium alloy wheel formed by backward extrusion [J]. Journal of Materials Research and Technology, 2023, 23: 4211−4225.

[7] WANG Qiang, ZHANG Zhi-min, YU Jian-min, XUE Yong. A novel backward extrusion process through rotating die and open punch [J]. Procedia Engineering, 2017, 207: 383−388.

[8] JIANG Yan-chao, ZHU Ya-tong, LE Qi-chi, LIAO Qi-yu, YIN Zhao-yang, ZHANG Xin-yue, WANG Ping. Finite element simulation and industrial validation for DRX evolution of magnesium alloy thin-walled wheel formed by backward extrusion [J]. Thin-Walled Structures, 2024, 197: 111567.

[9] ZHAN Mei, YANG He, GUO Jing, WANG Xian-xian. Review on hot spinning for difficult-to-deform lightweight metals [J]. Transactions of Nonferrous Metals Society of China, 2015, 25: 1732−1743.

[10] BI Da-sen, YANG Guang, CHU Liang, ZHANG Jian, WANG Zhi-hua. Numerical simulation on spinning forming process of automotive wheel rim [J]. Materials Science Forum, 2012, 704/705: 1458−1464.

[11] LIANG Wei, GUAN Lin, LV Qiong-ying, XING Zhi-gang. Research on multipass hot spinning process technology of AZ80 magnesium alloy shell [J]. Advances in Materials Science and Engineering, 2019, 2019: 8930134.

[12] XU Yi-wei, ZHAO Chun-jiang, WANG Qiang, QIU Yun-long, TIAN Wang, LI Shao-lu, ZHAO Ning, ZHAO Xiao-song. Ultra-low stress triaxiality ring-roller spinning: Microstructure, plastic behavior, and cumulative large deformation mechanism [J]. Journal of Materials Processing Technology, 2024, 324: 118240.

[13] MURATA M, KUBOKI T, MURAI T. Compression spinning of circular magnesium tube using heated roller tool [J]. Journal of Materials Processing Technology, 2005, 162/163: 540−545.

[14] HADADZADEH A, MOKDAD F, WELLS M A, CHEN D L. A new grain orientation spread approach to analyze the dynamic recrystallization behavior of a cast-homogenized Mg−Zn−Zr alloy using electron backscattered diffraction [J]. Materials Science and Engineering: A, 2018, 709: 285−289.

[15] WANG Qing-hang, ZHAI Hao-wei, LIU Lin-tao, XIA Hong-bo, JIANG Bin, ZHAO Jun, CHEN Dao-lun, PAN Fu-sheng. Novel Mg−Bi−Mn wrought alloys: The effects of extrusion temperature and Mn addition on their microstructures and mechanical properties [J]. Journal of Magnesium and Alloys, 2022, 10: 2588−2606.

[16] WANG Xiao-xia, GAO Ming, MIAO Lei, TAN Li-li, YANG Ke. Study of rotational dynamic recrystallization during warm compression of an Mg−Zn−Nd−Zr alloy [J]. Materials Today Communications, 2024, 38: 107928.

[17] NIENABER M, BOHLEN J, YI S B, KURZ G, KAINER K U, LETZIG D. Influence of Ca addition on the dynamic and static recrystallization behavior of direct extruded flat profiles of Mg−Y−Zn alloy [J]. Journal of Magnesium and Alloys, 2023, 11: 3736−3748.

[18] WANG Qing-hang, WANG Li, XU Jia-ze, ZHAI Hao-wei, CHEN Yang, XIA Shou-xin, QIN Xu, LI Yong-fei, JIANG Bin, CHEN Dao-lun. Extrusion limit diagram of Mg−5Bi−

3Al−1Zn alloy and effects of extrusion parameters on its microstructures and mechanical properties [J]. Journal of Materials Research and Technology, 2024, 29: 5166−5179.

[19] LI Min-hao, LU Li-wei, FAN Yu-tian, MA Min, WU Zhi-qiang, ZHOU Tao, QI Fu-gang, ZHANG Hua. Microstructure evolution and deformation behaviors of AZ31 Mg alloy sheets processed by repeated bending−flattening deformation with different die angles [J]. Transactions of Nonferrous Metals Society of China, 2024, 34: 812−832.

[20] PAN Jin-qi, ZHANG Wen-cong, LI Huan, YANG Jian-lei, ZHANG Zan, WANG Song-hui. Microstructure characteristics, yield asymmetry and fracture mechanism of the fine grained thin-wall Mg−6.03Zn−0.55Zr tubes fabricated by hot spinning [J]. Journal of Alloys and Compounds, 2024, 983: 173841.

[21] ZHAI Hao-wei, WANG Li, WANG Qing-hang, LI Meng, CHAI Yan-fu, XU Jun, JIANG Bin. Achieving high strength near 400 MPa in an ultra-fine grained Mg−Bi−Ca ternary alloy via low-temperature extrusion [J]. Journal of Materials Research and Technology, 2023, 26: 3973−3991.

[22] ROBSON J D, HENRY D T, DAVIS B. Particle effects on recrystallization in magnesium–manganese alloys: Particle-stimulated nucleation [J]. Acta Materialia, 2009, 57: 2739−2747.

[23] GUAN Di-kai, RAINFORTH W M, GAO Jun-heng, SHARP J, WYNNE B, MA Le. Individual effect of recrystallisation nucleation sites on texture weakening in a magnesium alloy: Part 1—Double twins [J]. Acta Materialia, 2017, 135: 14−24.

[24] GUAN Di-kai, RAINFORTH W M, GAO Jun-heng, MA Le, WYNNE B. Individual effect of recrystallisation nucleation sites on texture weakening in a magnesium alloy: Part 2—Shear bands [J]. Acta Materialia, 2018, 145: 399−412.

[25] YANG Xin-ye, WANG Peng, HUANG Ming. Grain boundary evolution during low-strain grain boundary engineering achieved by strain-induced boundary migration in pure copper [J]. Materials Science and Engineering: A, 2022, 833: 142532.

[26] MAO Hong, LIANG Qing-tao, ZHANG Zhi-kang, DU Yong, SHUAI Xiong, ZHANG Geng, TANG Sai. Strain-induced grain boundary migration and grain rotation in polycrystalline metals: Atomic- and meso-scale phase field simulations [J]. Computational Materials Science, 2023, 230: 112531.

[27] LIU Ru-xue, LI Kai, ZHOU Guo-wei, TANG Wei-qin, SHEN Yao, TANG Ding, LI Da-yong. Simulation of strain induced abnormal grain growth in aluminum alloy by coupling crystal plasticity and phase field methods [J]. Transactions of Nonferrous Metals Society of China, 2022, 32: 3873−3886.

[28] LUO Lin, CHENG Wei-li, YU Hui, WANG Hong-xia, NIU Xiao-feng, WANG Li-fei, LI Hang, YOU Zhi-yong, HOU Hua. Dynamic recrystallization behavior and strengthening mechanism of quasi-precipitate-free dilute Mg−Bi−Sn alloy [J]. Materials Science and Engineering: A, 2022, 850: 143553.

[29] WANG Qing-hang, JIANG Bin, TANG Ai-tao, HE Chao, ZHANG Ding-fei, SONG Jiang-feng, YANG Tian-hao, HUANG Guang-sheng, PAN Fu-sheng. Formation of the elliptical texture and its effect on the mechanical properties and stretch formability of dilute Mg−Sn−Y sheet by Zn addition [J]. Materials Science and Engineering: A, 2019, 746: 259−275.

[30] YI S B, BROKMEIER H G, LETZIG D. Microstructural evolution during the annealing of an extruded AZ31 magnesium alloy [J]. Journal of Alloys and Compounds, 2010, 506: 364−371.

[31] GAUTAM P C, BISWAS S. On the possibility to reduce ECAP deformation temperature in magnesium: Deformation behaviour, dynamic recrystallization and mechanical properties [J]. Materials Science and Engineering: A, 2021, 812: 141103.

[32] WANG Kui, WANG Jing-feng, HUANG Song, DOU Xiao-xu, WANG Jin-xing, WANG Cun-long. Formation of an abnormal texture in Mg−Gd−Y−Zn−Mn alloy and its effect on mechanical properties by altering extrusion parameters [J]. Materials Science and Engineering: A, 2022, 831: 142270.

[33] LEE J Y, YUN Y S, KIM W T, KIM D H. Twinning and texture evolution in binary Mg−Ca and Mg−Zn alloys [J]. Metals and Materials International, 2014, 20: 885−891.

[34] SANJARI M, FARZADFAR A, KABIR A S H, UTSUNOMIYA H, JUNG I H, PETROV R, KESTENS L, YUE S. Promotion of texture weakening in magnesium by alloying and thermomechanical processing. I: Alloying [J]. Journal of Materials Science, 2014, 49: 1408−1425.

[35] GUTIÉRREZ C E J, HERNÁNDEZ M M G, SALINAS R A, AGUILAR C J, REYES D I. An EBSD investigation on the columnar grain growth in non-oriented electrical steels assisted by strain induced boundary migration [J]. Materials Letters, 2019, 252: 42−46.

[36] XIONG Xun-fei, ZENG Ying, FU Rui-hao, LIU Man-ping, JIANG Bin. The quantitative regulation of basal and prismatic Mg_2Sn to strengthen Mg−Sn alloys [J], Journal of Alloys and Compounds 2024, 997: 174615.

[37] JIANG M G, XU C, YAN H, FAN G H, NAKATA T, LAO C S, CHEN R S, KAMADO S, HAN E H, LU B H. Unveiling the formation of basal texture variations based on twinning and dynamic recrystallization in AZ31 magnesium alloy during extrusion [J]. Acta Materialia, 2018, 157: 53−71.

[38] WANG Tao, YANG Lun, TANG Zhao-feng, WU Lei, YAN Huan-yuan, LIU Chao, MA Yun-zhu, LIU Wen-sheng, YU Zhao-ji. Microstructure, mechanical properties and deformation mechanism of powder metallurgy AZ31 magnesium alloy during rolling [J]. Materials Science and Engineering: A, 2022, 844: 143042.

[39] LIU Zhan, NIE Jin-feng, ZHAO Yong-hao. Effect of deformation processing on microstructure evolution and mechanical properties of Mg−Li alloys: A review [J]. Transactions of Nonferrous Metals Society of China, 2024, 34: 1−25.

[40] ZHAO Jun, FU Jie, JIANG Bin, TANG Ai-tao, SHENG Hao-ran, YANG Tian-hao, HUANG Guang-sheng, ZHANG Ding-fei, PAN Fu-sheng. Influence of Li addition on the microstructures and mechanical properties of Mg−Li alloys [J]. Metals and Materials International, 2021, 27: 1403−1415.

[41] WANG Song-hui, YANG Jian-lei, PAN Jin-qi, WANG

Hai-xuan, ZHANG Wen-cong, SUN You-ping, DAI Xiang-yu, CHEN Wen-zhen, CUI Guo-rong, CHU Guan-nan. Unveiling the mechanical response and deformation mechanism of extruded Mg−2.5Nd−0.5Zn−0.5Zr alloy sheet under high-temperature tensile [J]. Journal of Alloys and Compounds, 2022, 911: 164987.

[42] SUH B C, KIM J H, BAE J H, HWANG J H, SHIM M S, KIM N J. Effect of Sn addition on the microstructure and deformation behavior of Mg−3Al alloy [J]. Acta Materialia, 2017, 124: 268−279.

[43] CHEN Yang, WANG Qing-hang, WANG Li, ZHAI Hao-wei, HUANG Li-xin, JIANG Bin, MAO Yong, HE Jun-jie. Deformation mechanisms of as-extruded Mg−3Bi−1Ca (wt.%) alloy during room-temperature tension [J]. Materials Science and Engineering: A, 2023, 875: 145119.

[44] NEWBURY D E, WILLIAMS D B. The electron microscope: The materials characterization tool of the millennium [J]. Acta Materialia, 2000, 48: 323−346.

[45] WANG Sen, PAN Hu-cheng, XIE Dong-sheng, ZHANG Dong-dong, LI Jing-ren, XIE Hong-bo, REN Yu-ping, QIN Gao-wu. Grain refinement and strength enhancement in Mg wrought alloys: A review [J]. Journal of Magnesium and Alloys, 2023, 11: 4128−4145.

[46] YANG Yan, XIONG Xiao-ming, CHEN Jing, PENG Xiao-dong, CHEN Dao-lun, PAN Fu-sheng. Research advances of magnesium and magnesium alloys worldwide in 2022 [J]. Journal of Magnesium and Alloys, 2023, 11: 2611−2654.

镁合金轮毂的动态再结晶行为及旋压织构形成机制

姜炳春[1,2]，翟浩巍[3]，王庆航[3,4]，李 蒙[4]，张 彤[1,2]，蒋 斌[5]

1. 广东科技学院 机电工程学院，东莞 523083；
2. 澳门中西学院 数字科学与技术学院，澳门 999078；
3. 扬州大学 机械工程学院，扬州 225127；
4. 中信戴卡股份有限公司，秦皇岛 066000；
5. 重庆大学 材料科学与工程学院 国家镁合金材料工程技术研究中心，重庆 400044

摘 要：研究了在旋压过程中 AZ31 镁合金轮毂的动态再结晶行为及织构形成机制。光学显微镜、电子背散射衍射、透射电子显微镜及有限元模拟分析结果表明，在整个旋压过程中，连续动态再结晶机制与晶界弓出机制共同作用，增加了动态再结晶晶粒区域面积。研究还发现，形变母晶的取向大部分被新形成的动态再结晶晶粒继承。旋压过程主要分为两个阶段：在初始阶段，当滚轮接触合金并移至最低点时，变形机制主要由基面⟨*a*⟩滑移驱动；在后续阶段，随着沿旋压方向施加外力，变形机制转变为以锥面⟨*c*+*a*⟩滑移为主，最终形成晶体 *c* 轴向旋压方向倾斜±15°的织构。这一织构导致旋压方向和横向拉伸性能的各向异性。

关键词：镁合金轮毂；动态再结晶；旋压织构；位错滑移；力学性能各向异性

(Edited by Wei-ping CHEN)